Classical and quantum metrology of the Lieb-Liniger model

Jae-Gyun Baak and Uwe R. Fischer

Department of Physics and Astronomy, Seoul National University, Center for Theoretical Physics, Seoul 08826, Korea

We study the classical and quantum Fisher information of the interaction coupling in the Lieb-Liniger model. Fisher information has been studied extensively when the parameter is inscribed on a quantum state by a unitary process, e.g., Mach-Zehnder or Ramsey interferometry. Here we investigate the case that a Hamiltonian parameter to be estimated is imprinted on eigenstates of that Hamiltonian and thus is not necessarily encoded by a unitary operator. We take advantage of the fact that the Lieb-Liniger model is exactly soluble for both periodic and hard-wall boundary conditions. For the latter case, we provide a derivation of the explicit expression for the norm of the Lieb-Liniger wave function. The Fisher information is determined for various small numbers of particles, for both ground state and excited states of type I and type II in the Lieb-Liniger terminology. We discuss the dependence of the Fisher information on interaction strength and system size, to further evaluate the metrological aspects of the model. Particularly noteworthy is the fact that the Fisher information displays a maximum when we vary the system size, indicating that the distinguishability of the wave functions is largest when the Lieb-Liniger parameter is at the crossover between Bose-Einstein condensate and Tonks-Girardeau limits. The saturability of this Fisher information by employing standard absorption imaging as the measurement method is assessed by a specific modeling of the latter.

I. INTRODUCTION

The Lieb-Liniger (LL) model is the archetype of an exactly soluble many-body problem with direct experimental relevance [1,2]. It describes N bosons interacting via a repulsive contact interaction in one-dimensional space. The time-independent Schrödinger equation with the LL Hamiltonian has been solved by the method of coordinate Bethe ansatz [3,4] with varying boundary conditions [5,6]: Periodic and hard-wall boundary conditions, which correspond to the particles moving along a ring and in a flat box, respectively. The characteristic behavior of the energy spectrum and the eigenstates of this model has been studied over the years in many guises; see, for example, Refs. [6–12]. The theoretical analyses of many-body systems have focused on special regimes of parameters such as thermodynamic limit, weakly and strongly interacting regimes due to their relative ease of capturing the physical features inherent to the systems [13–15]. One notable case is that the type II elementary excitations in the LL model have been revealed to have correspondence to the dark solitons of the Gross-Pitaevskii equation in the weak interaction limit [16–21]. On the other hand, there have been trials, often using the multiconfigurational Hartree method, to approach the regime where the interaction strength is intermediate between its two extremes or only a few particles are involved without thermodynamic limit [13,22–24]. Here we focus on the Fisher information for the interaction strength calculated with respect to the LL eigenstates with a few particles.

The Fisher information indicates the distinguishability of a physical state by some measurement when a state parameter slightly changes. It determines a minimum distance in the parameter space for different states to be resolved, and only if the change of parameter value is larger than this distance, one can detect the variation of state by the corresponding measurement [25]. Thus the classical Fisher information (CFI) for a given measurement defines the precision limit of estimating a parameter imprinted on a state, and the quantum Fisher information (QFI) is the maximized CFI when an optimal measurement is assumed. All of the above is succinctly formulated by the combined classical-quantum Cramér-Rao inequalities [26–30]:

$$\langle(\delta\theta_{\text{est}})^2\rangle_\theta \geqslant \frac{1}{MF(\theta)} \geqslant \frac{1}{M\mathfrak{F}(\theta)}, \tag{1}$$

where θ_{est} is an estimator mapping M measurement outcomes to an estimate for a parameter θ, and $\delta\theta_{\text{est}}$ is the bias-corrected deviation from the true value of θ: $\theta_{\text{est}}/|d\langle\theta_{\text{est}}\rangle_\theta/d\theta| - \theta$. The second inequality, which provides the tighter bound, represents the quantum version of the first one which gives the classical Cramér-Rao bound. The expectation value of $(\delta\theta_{\text{est}})^2$ with respect to a state with θ as a true value is denoted by $\langle(\delta\theta_{\text{est}})^2\rangle_\theta$. Also, $F(\theta)$ and $\mathfrak{F}(\theta)$ represent the CFI and the QFI for the estimation of θ, respectively. The first inequality in Eq. (1) is always asymptotically, i.e., as $M \to \infty$, saturable by using the maximum likelihood estimator (MLE) for θ_{est}, and the second inequality can always be saturated theoretically by finding the optimal measurement [27,28].

Quantum parameter estimation theory concerns estimating a parameter θ in a Hamiltonian H_θ and suggests the general measurement scheme consisting of four steps [31]: (1) the preparation of an initial quantum state, say, ρ_0, (2) the imprint of a parameter on the state during its physical process, where

typically $\rho_\theta = U_\theta \rho_0 U_\theta^\dagger$ with a unitary operator U_θ derived from H_θ, (3) the measurement of the final state ρ_θ, and after repeating these three steps M times, (4) the estimation of the parameter θ from those M measurement results. Numerous studies have investigated how to improve the N-scaling of the QFI in this protocol, where N is the number of available quantum resources such as equally prepared quantum states or the number of particles. The aim is to surpass the standard quantum (shot noise) limit, $\mathfrak{F}(\theta) \sim N$, and ultimately achieve the Heisenberg limit, $\mathfrak{F}(\theta) \sim N^2$. The enhancement of the N-scaling implies an improved measurement precision with the same amount of resource (N copies of some fundamental entity), and can be theoretically accomplished by preparing special initial states, which are commonly entangled or squeezed, in step (1) [30,32–34] or utilizing various dynamics during the state evolution in step (2) [35–37]. Such studies that concentrate on the QFI assume the saturability of $F(\theta) \leqslant \mathfrak{F}(\theta)$ by choosing the optimal measurements in step (3). However, these theoretically obtained measurements are usually distant from those implemented in the real experiments except for a few cases like spin measurement in the magnetic field [38]. Thus the actual precision is often evaluated by the CFI on the basis of the realistic measurements such as the measurement of population imbalance between two possible outputs [39,40].

The framework of quantum metrology so far has mainly been discussed within the SU(2) representation, which mathematically describes the two-state systems like two polarization states of a photon, two spin states of a spin-1/2 atom, and two locations of an atom in a double-well potential. Then two-mode interferometric methodology, e.g. Mach-Zehnder or Ramsey interferometry, makes use of the interference between two internal states or two spatially separated states in order to extract the relative phase between the two states, from which one can estimate the target parameters. Particularly, the quantum metrology with the ultracold bosonic gas such as Bose-Einstein condensates (BECs) in a double-well trap has been vastly studied [39,41–45]. Such metrology using the trapped atomic systems depends on the validity of two-mode approximation, the conditions of which include small interparticle interaction or sufficient separation of the two wells in a double-well potential [46]. Even in the case of bosons in a single harmonic trap, the SU(2) metrology can be applied if one can assume the regimes of parameters where the two-mode approximation effectively describes the dynamics of the systems [47].

In this paper, we analyze the metrological scenario of estimating a Hamiltonian parameter using the eigenstates of that Hamiltonian, which naturally contain the parameter to be estimated in a nonunitary way. This scenario is involved in a single state, especially in the position representation, thus the interference between any two states is not taken into account, whereas in the SU(2) scenario the superposition of two orthogonal states is used to produce the relative phase originating from the distinct evolutions of those states under a unitary process. The estimation efficiency is evaluated by the Fisher information defined in terms of the wave function, and we concentrate on the analysis of the wave function-based Fisher information itself rather than its N-scaling. All of these are discussed with the LL model, where the position

measurement of the particles is chosen to calculate the CFI and evaluate the precision of estimating the interaction strength. Instead of finding the optimal measurements, we discuss the conditions under which the position measurement is optimal and try to assess the realistic measurement precision based on the absorption imaging of atomic cloud, which is shown to be the imperfect version of the position measurement.

This paper is organized as follows. In Sec. II we look through the LL model including the eigenfunctions and their norms, which are necessary to calculate the Fisher information, under two different boundary conditions: Periodic and hard-wall boundary conditions. In Sec. III A we first introduce the appropriate forms of CFI and QFI in terms of the wave function and relate the saturability of $F(\theta) \leqslant \mathfrak{F}(\theta)$ to certain class of wave functions. Then we construct a mathematical model of the imperfect measurement of the particle positions in order to simulate the absorption imaging method, which is the main measurement tool to explore the ultracold atomic systems [48,49]. Last we develop the formula of Fisher information for the interaction strength calculated with respect to the LL eigenfunctions and discuss its functional properties. Also, the issue of computing the scalar product between two LL eigenstates that one encounters while calculating the Fisher information is explained. In Sec. IV the Fisher information thus obtained is plotted versus the interaction strength or the system size, and several notable features are discussed. We consider the effect of the number of particles and the types of elementary excitations on the Fisher information. In every case, the Fisher information values for two different boundary conditions are compared. Finally we show that the precision limit defined by the Fisher information can be achieved by the absorption imaging as its resolution improves.

II. LIEB-LINIGER MODEL UNDER DIFFERENT BOUNDARY CONDITIONS

The one-dimensional dynamics of N bosons interacting via a repulsive δ-function potential is described by the LL Hamiltonian

$$\hat{H}_{\mathrm{LL}} = -\sum_{j=1}^{N} \frac{\partial^2}{\partial x_j^2} + 2c \sum_{j<l} \delta(x_j - x_l), \qquad (2)$$

where $c > 0$ due to the repulsion and $\hbar = 2m = 1$. To fix the units, we also express c in terms of the inverse of an arbitrarily chosen length scale. The time-independent Schrödinger equation, $\hat{H}_{\mathrm{LL}} \psi = E \psi$, is solved by the Bethe method with appropriate boundary conditions [5,6]. The procedure of the Bethe method is as follows: (1) Under the initial assumption that any two particles do not move across each other, each particle is regarded as a free particle. Hence the functional form of the *Bethe ansatz* is given by the superposition of free particle wave functions in the domain $D : x_1 < x_2 < \cdots < x_N$. (2) The δ-function potential gives a continuity equation, $[\partial \psi / \partial x_{j+1} - \partial \psi / \partial x_j = 2 c \psi]|_{x_{j+1}=x_j}$, determining the form of coefficients in the Bethe ansatz. (3) Applying the boundary condition introduces the system size, L, and leads to the *Bethe equations* which determine the *quasimomenta* introduced by the free particle wave functions. The

N-boson wave functions must be symmetric under the exchange of arbitrary two spatial coordinates, thus the Bethe ansatz defined only in the domain D so far covers the entire space, $[0, L]^N$. Now we have the exact LL eigenfunctions. (4) In addition to these, however, we devote our particular attention to the norm of Bethe ansatz, hence we explicitly represent the norm of LL eigenfunction under a given boundary condition.

The most well-known solution of the LL model is the one under the periodic boundary condition describing the one-dimensional system of N bosons moving along a ring. The Bethe ansatz for this boundary condition is given by

$$\tilde{\psi}(x_1, \ldots, x_N) = \sum_{P's} A(P) \, e^{i \sum_{j=1}^N k_{P_j} x_j}, \tag{3}$$

where the continuity equation gives

$$A(P) = \prod_{j<l} \left(1 + \frac{ic}{k_{P_j} - k_{P_l}} \right).$$

The tilde of $\tilde{\psi}$ in Eq. (3) emphasizes that it is unnormalized. The sum over P's means the sum over a set of the permutations of the integers from 1 to N. The energy and the momentum of the state described by this wave function are $E_N = \sum_{j=1}^N k_j^2$ and $P_N = \sum_{j=1}^N k_j$, respectively. Then applying the periodic boundary condition introduces the system size L by imposing the cyclicity condition on the wave function, $\tilde{\psi}(x_1, \ldots, x_N) = \tilde{\psi}(x_2, \ldots, x_N, x_1 + L)$, which is now defined in the domain $D' : 0 < x_1 < \cdots < x_N < L$. From this condition, one obtains a system of N equations, i.e., Bethe equations:

$$L k_j = 2\pi I_j - 2 \sum_{l=1}^N \tan^{-1} \left(\frac{k_j - k_l}{c} \right), \tag{4}$$

which relate the quasimomenta k_j's to the values of I_j's given c and L. The quantum numbers, $I_1 < I_2 < \cdots < I_N$, are half-integers for even N or integers for odd N and do not allow duplicate values. The symmetric distribution of I_j's around 0 with interval 1, $[I_1 = -(N-1)/2, I_2 = -(N-3)/2, \ldots, I_N = (N-1)/2]$, gives the symmetric distribution of k_j's around 0, which obviously minimizes the energy. Thus it corresponds to the ground state with minimal energy and zero momentum. The norm of the unnormalized wave function in Eq. (3) has been conjectured in Ref. [10] and proved in Ref. [50] using the method of algebraic Bethe ansatz. The norm squared of Eq. (3) has thus been established to be

$$\mathcal{N}^2 = \prod_{j<l} \left(1 + \frac{c^2}{(k_j - k_l)^2} \right) \det[\mathbf{H}], \tag{5}$$

where the entries of the Hessian matrix $\mathbf{H}$ are

$$[\mathbf{H}]_{ij} = \delta_{ij} \left(L + \sum_{l=1}^N \frac{2c}{(k_i - k_l)^2 + c^2} \right) - \frac{2c}{(k_i - k_j)^2 + c^2}.$$

The LL model with the hard-wall boundary condition has been covered in Refs. [6,8–10,12]. The Bethe ansatz for this boundary condition is given by

$$\tilde{\psi}(x_1, \ldots, x_N) = \sum_{\epsilon's} \sum_{P's} \pi_\epsilon A(\epsilon, P) e^{i \sum_{j=1}^N \epsilon_j k_{P_j} x_j}, \tag{6}$$

where the continuity equation gives

$$A(\epsilon, P) = \prod_{j<l} \left[1 - \frac{ic}{\epsilon_j k_{P_j} + \epsilon_l k_{P_l}} \right] \left[1 + \frac{ic}{\epsilon_j k_{P_j} - \epsilon_l k_{P_l}} \right].$$

Here $\epsilon := \{\epsilon_1, \ldots, \epsilon_N\}$ and each ϵ_j is summed over ± 1. The P runs over all permutations of $[1, 2, \ldots, N]$ as in Eq. (3) and π_ϵ is the product of all the ϵ_j's: $\epsilon_1 \epsilon_2 \cdots \epsilon_N$. The sign of k_j is absorbed into ϵ_j to make $k_j > 0$ $\forall j$ and $k_1 < k_2 < \cdots < k_N$ is assumed without loss of generality due to the sum over P's. The application of the hard-wall boundary condition introduces the system size L by imposing a condition on the wave function, $\tilde{\psi}(x_1 = 0, x_2, \ldots, x_N) = \tilde{\psi}(x_1, \ldots, x_{N-1}, x_N = L) = 0$, which is now defined in the domain D'. This condition finally gives the Bethe equations for quasimomenta:

$$L k_j = \pi I_j - \sum_{l \neq j} \left[\tan^{-1} \left(\frac{k_j - k_l}{c} \right) + \tan^{-1} \left(\frac{k_j + k_l}{c} \right) \right]. \tag{7}$$

The quantum numbers, $I_1 < I_2 < \cdots < I_N$, are positive integers irrespective of the evenness of N and do not allow duplicate values, thus the ground state corresponds to $[I_1 = 1, I_2 = 2, \ldots, I_N = N]$, which minimizes the energy $E_N = \sum_{j=1}^N k_j^2$. Applying the conjecture about the norm of Bethe ansatz in Ref. [10] to Eq. (7) leads to the norm squared of Eq. (6) being expressible as

$$\mathcal{N}^2 = 2^N \prod_{j<l} \left[1 + \frac{c^2}{(k_j - k_l)^2} \right] \left[1 + \frac{c^2}{(k_j + k_l)^2} \right] \det[\mathbf{H}(B)]. \tag{8}$$

See for a derivation the Appendix, where this norm is Eq. (A11), and where $\mathbf{H}(B)$ is the Hessian matrix of the function $B(k_1, \ldots, k_N)$, provided by Eqs. (A12) and (A10) of the Appendix, respectively. We display the contour plots of the wave function for $c = 0.2$ and $c = 1.1$ and for both periodic and hard-wall boundary conditions in Fig. 1.

The LL model under either of the boundary conditions above is fully described by three parameters: Interaction strength c, system size L, and particle number N. If one considers, however, the dimensionless form of the LL model, $k_j \to \tilde{k}_j = L k_j$, $c \to \tilde{c} = c L$, and $x_j \to \tilde{x}_j = x_j/L$, one can find that the system depends only on the two parameters: cL and N. Basically this origins from the characteristics of Bethe equations, Eq. (4) and Eq. (7), that for fixed N the Bethe equations are invariant under any change of c and L keeping cL constant. Hence for a fixed number of particles, the value of $\tilde{c} = cL$ completely determines the value of $\tilde{k}_j = Lk_j$ and thus the system. In thermodynamic limit, $N \to \infty$ with N/L fixed, the LL model is completely described by a single parameter called the Lieb parameter: $\gamma = c/\rho$, where ρ is the number density N/L. Also, in this limit, the different effects between the two boundary conditions disappear and even the properties of bosonic gas along a ring space can be considered as if the gas resides in a flat box potential.

Though a dimensionless form helps to understand the essence of a system irrespective of the unit choice for the parameters, in order to test and apply the Fisher information as a realistic indicator for the limit of measurement precision, we don't take such dimensionless parameters so that c and L
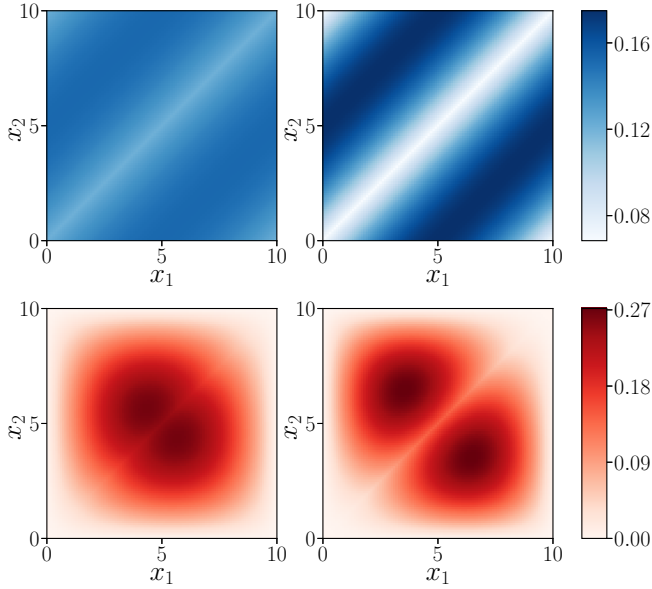
FIG. 1. The normalized ground-state wave functions of $N = 2$ particles in the LL model under periodic boundary condition (upper row) and hard-wall boundary condition (lower row) with interaction strength $c = 0.2$ (left) and $c = 1.1$ (right). One can see how different geometries defined by boundary conditions are reflected in the wave function profiles. When c is small, the two particles are more likely to share a common space, while they move away from each other as c increases. Between the two extreme limits of c, $c = 0$ and $c = \infty$, there appears a maximum sensitivity of the wave function with respect to c, which is reflected in the larger Fisher information in that region, which forms a major focus of the present study.

can be treated separately. By doing so, we can verify how the independent adjustment of one parameter can help improve the measurement precision of the other, thus we can simulate the situations encountered in the real measurements. Also, we don't assume thermodynamic limit and keep small number of particles to investigate the role of different geometries specified by different boundary conditions: Periodic and hard-wall boundary conditions. Hence the system is now described by three independent parameters: c, L, and N.

III. FISHER INFORMATION IN THE LIEB-LINIGER MODEL

A. Fisher information of the wave function

The Fisher information has played an important role in the parameter estimation theory in that it determines the precision to which one can fundamentally estimate a parameter encoded in a probability distribution. For any conditional probability density $P(X|\theta)$ of a continuous random variable X, the CFI of a parameter θ is

$$F(\theta) = \int dx \, \frac{1}{P(x|\theta)} \left(\frac{\partial P(x|\theta)}{\partial \theta} \right)^2, \qquad (9)$$

where the integral (or sum for a discrete random variable) is done over the domain of a single measurement result x. The $F(\theta)$ quantifies how well two slightly different values of θ can be distinguished based on a single measurement outcome

x. When a set of M outcomes from M independently and identically repeated measurements is used to estimate the θ, the inverse of $\sqrt{MF(\theta)}$ provides the lower limit of estimation error as in Eq. (1).

In quantum theory, a quantum state parametrized by a parameter θ is connected to a probability distribution of the measurement results by $P(x|\theta) = \text{Tr}[\rho_\theta \hat{E}_x]$, where ρ_θ is the quantum state and a set of $\hat{E}_x$ for all possible x, $\{\hat{E}_x : x\}$, is the positive operator-valued measure (POVM) specifying the type of measurement. Given ρ_θ, the $\text{Tr}[\rho_\theta \hat{E}_x]$ allows additional optimization over the POVMs in a way that $F(\theta)$ is maximized. The maximal $F(\theta)$ defines the QFI of θ:

$$\mathfrak{F}(\theta) = \max_{\{\hat{E}_x : x\}} F(\theta) = \text{Tr}[\rho_\theta L_\theta^2], \qquad (10)$$

where L_θ is the symmetric logarithmic derivative satisfying $\partial_\theta \rho_\theta = (\rho_\theta L_\theta + L_\theta \rho_\theta)/2$. By Eq. (1), the QFI specifies the precision one can ultimately attain for estimating an unknown parameter encoded in a quantum state. Note that the optimal POVM making $F(\theta)$ reach its maximum can always be found. When the parameter θ is encoded by a unitary process with some generator $\hat{G}$, $\rho_\theta = e^{-i\theta \hat{G}} \rho_0 \, e^{i\theta \hat{G}}$, the upper bound of QFI is given as $4\langle \psi_0|(\Delta G)^2|\psi_0\rangle$, which obviously can be reached when ρ_0 is a pure state: $\rho_0 = |\psi_0\rangle\langle\psi_0|$. Thus, for general states including mixed ones, $\mathfrak{F}(\theta) \leqslant 4\langle \psi_0|(\Delta G)^2|\psi_0\rangle$ [29].

Here, however, we are concerned with the Fisher information of a Hamiltonian parameter that a quantum state naturally has after being realized as an eigenstate of that Hamiltonian rather than unitarily encoded. For the generic pure state $|\psi_\theta\rangle$ with θ encoded via a physical process, the QFI defined in Eq. (10) reduces to

$$\mathfrak{F}(\theta) = 4 \left(\langle \partial_\theta \psi_\theta | \partial_\theta \psi_\theta \rangle - |\langle \psi_\theta | \partial_\theta \psi_\theta \rangle|^2 \right)$$

$$= 4 \left(\int d\mathbf{x} \, |\partial_\theta \psi_\theta(\mathbf{x})|^2 - \left| \int d\mathbf{x} \, \psi_\theta^*(\mathbf{x}) \, \partial_\theta \psi_\theta(\mathbf{x}) \right|^2 \right), \quad (11)$$

where it is also expressed in the position representation with an N-particle position state $|\mathbf{x}\rangle := |x_1, x_2, \ldots, x_N\rangle$ satisfying $\int d\mathbf{x}|\mathbf{x}\rangle\langle\mathbf{x}| = \hat{1}$ and $\langle\mathbf{x}|\mathbf{x}'\rangle = \delta(\mathbf{x} - \mathbf{x}')$. When $\psi_\theta(\mathbf{x})$ is the most general complex-valued function, we can consider the polar representation of a wave function: $\psi_\theta(\mathbf{x}) = |\psi_\theta(\mathbf{x})|e^{i\varphi_\theta(\mathbf{x})}$, with some real-valued function $\varphi_\theta(\mathbf{x})$. Then $\mathfrak{F}(\theta)$ in Eq. (11) can be further transformed into

$$\frac{\mathfrak{F}(\theta)}{4} = \int d\mathbf{x} \, (\partial_\theta |\psi_\theta(\mathbf{x})|)^2 + \int d\mathbf{x} \, |\psi_\theta(\mathbf{x})|^2 (\partial_\theta \varphi_\theta(\mathbf{x}))^2$$

$$- \left(\int d\mathbf{x} \, |\psi_\theta(\mathbf{x})|^2 \, \partial_\theta \varphi_\theta(\mathbf{x}) \right)^2, \qquad (12)$$

where $\int d\mathbf{x} \, |\psi_\theta(\mathbf{x})| \, \partial_\theta |\psi_\theta(\mathbf{x})| = 0$ derived from the θ derivative of $\int d\mathbf{x} \, |\psi_\theta(\mathbf{x})|^2 = 1$ is used. The second and third terms in Eq. (12) combine to be the variance of $\partial_\theta \varphi_\theta(\mathbf{x})$ with respect to the probability distribution $P(\mathbf{x}|\theta) = |\psi_\theta(\mathbf{x})|^2$. On the other hand, the CFI in Eq. (9) can be recast in terms of the wave function by the relation $P(\mathbf{x}|\theta) = |\psi_\theta(\mathbf{x})|^2$:

$$F(\theta) = 4 \int d\mathbf{x} \, (\partial_\theta |\psi_\theta(\mathbf{x})|)^2, \qquad (13)$$

and finally it obviously follows that the QFI in Eq. (12) comprises two parts [51,52]:

$$\mathfrak{F}(\theta) = F(\theta) + 4\,\mathrm{Var}[\partial_\theta \varphi_\theta]_{\psi_\theta}, \qquad (14)$$

in which $\mathrm{Var}[A]_{\psi_\theta}$ means the variance of a quantity $A(\mathbf{x})$ with respect to the probability distribution $|\psi_\theta(\mathbf{x})|^2$.

To represent the CFI in terms of the wave function implies that a set of $\hat{E}_{\mathbf{x}} = |\mathbf{x}\rangle\langle\mathbf{x}|$, i.e., $\{|\mathbf{x}\rangle\langle\mathbf{x}| : \mathbf{x}\}$, is chosen as a POVM, which means the projective measurement of the positions of N particles. This POVM is not optimal according to Eq. (14), but we can find it optimal under certain conditions. One notable case is when $\psi_\theta(\mathbf{x}) = e^{i\varphi(\theta)}\phi_\theta(\mathbf{x})$ with $\varphi(\theta)$ and $\phi_\theta(\mathbf{x})$ being real-valued. Since $\varphi(\theta)$ is independent of $\mathbf{x}$, the variance term in Eq. (14) disappears, hence $\mathfrak{F}(\theta) = 4\int d\mathbf{x}\,[\partial_\theta \phi_\theta(\mathbf{x})]^2 = F(\theta)$. For example, if $\psi_\theta(\mathbf{x})$ is real-valued, $\varphi(\theta) = 0$, or is purely imaginary-valued, $\varphi(\theta) = \pi/2$, the QFI will be $4\int d\mathbf{x}\,[\partial_\theta \psi_\theta(\mathbf{x})]^2$ or $-4\int d\mathbf{x}\,[\partial_\theta \psi_\theta(\mathbf{x})]^2$, respectively, which is exactly equal to the CFI calculated by Eq. (13) with the corresponding $\psi_\theta(\mathbf{x})$. If $\phi_\theta(\mathbf{x})$ is an eigenstate of a Hamiltonian, which can always be chosen to be real, then $e^{i\varphi(\theta)}\phi_\theta(\mathbf{x})$ is a representation of its time evolution, where $\varphi(\theta)$ contains the eigenenergy of the state that also relies on the Hamiltonian parameter θ. Thus the saturation of CFI to QFI is maintained along the time evolution. Finally, the Fisher information defined as above applies to the case when one tries to estimate a Hamiltonian parameter θ from the position measurement on the eigenstates of that Hamiltonian.

B. Single-shot measurement with finite resolution

The ultimate quantum limit of any measurement precision is identified by the QFI, but the feasible limit is always given by the CFI, that is, by a specific choice of measurement. Relating the probability density $P(x|\theta)$ to the wave function $\psi_\theta(x)$ introduces a (hypothetical) measurement where the positions of N particles are determined with infinite level of precision. Even though we have discussed the condition on $\psi_\theta(x)$ to make $\mathfrak{F}(\theta) = F(\theta)$, what one actually encounters in the real experiments is the imperfect measurement allowing for uncertainty in the measured positions, which can be supported by the absorption imaging method that has been used as a measurement to investigate the cold atomic systems [53]. This method is implemented by irradiating laser light from above to the cold atomic gas and measuring the brightness captured by the CCD camera installed below the gas. The brightness profile generated from the camera is fitted to obtain the column density distribution of the gas, hence this absorption imaging is thought of as a measurement of the number of particles in each pixel area of the camera. Then one can estimate any system parameter from the density profile. By using a model of single-shot measurement with finite resolution to simulate the absorption imaging [54–56], it can be shown that as narrowing the pixel size, one can asymptotically obtain the precision level provided by the perfect position measurement.

The imperfect measurement of the position of a single particle in one-dimensional space with finite resolution Δx_p is described by the POVM $\{\hat{\Pi}_j : j\}$ satisfying

$$\hat{\Pi}_j \coloneqq \int_{a_j}^{a_{j+1}} dx\,\hat{\Pi}(x), \quad \sum_j \hat{\Pi}_j = \int_{-\infty}^{\infty} dx\,\hat{\Pi}(x) = \mathbb{I}, \qquad (15)$$

where $\hat{\Pi}(x) = |x\rangle\langle x|$ forms a POVM for the perfect position measurement and $a_{j+1} - a_j = \Delta x_p\;\forall j$. It is easy to show that $\hat{\Pi}_j\,\hat{\Pi}_l = \delta_{jl}$, which is the property satisfied by the projective measurements. Thus the probability of finding a particle within a range (a_j, a_{j+1}), $\mathrm{Tr}[\rho_\theta \hat{\Pi}_j]$, is considered instead of the one of finding the particle exactly at x, $\mathrm{Tr}[\rho_\theta \hat{\Pi}(x)]dx$, for a given quantum state ρ_θ.

We extend this consideration to the case of N particles and N_p pixels. The coordinate range of jth pixel is denoted by $A_j \coloneqq (a_{j-1}, a_j)$, where $j = 0, 1, \ldots, N_p, N_p + 1$ and $a_j - a_{j-1} = \Delta x_p$ for all j's except for 0 and $N_p + 1$. Also, we define $a_{-1} \coloneqq -\infty$ and $a_{N_p+1} \coloneqq \infty$. A one-dimensional absorption image can be written as $\mathfrak{n} \coloneqq (\mathfrak{n}_0, \mathfrak{n}_1, \ldots, \mathfrak{n}_{N_p}, \mathfrak{n}_{N_p+1})$, where $\mathfrak{n}_{j\neq 0, N_p+1}$ is the number of atoms found in jth pixel bin and $\sum_{j=0}^{N_p+1} \mathfrak{n}_j = N$, i.e., the total number of particles. We assume the length $\Delta x_p N_p$ should be large enough to cover the whole system, but the numbers of atoms outside the measured area, $\mathfrak{n}_0$ for the left and $\mathfrak{n}_{N_p+1}$ for the right, are considered for theoretical completion.

Now one can think of the probability distribution of absorption images:

$$P(\mathfrak{n}|\theta) = \zeta_{\mathfrak{n}} \int_A d\mathbf{x}\,P(\mathbf{x}|\theta), \quad \sum_{\mathfrak{n}\in H(N,N_p)} P(\mathfrak{n}|\theta) = 1, \qquad (16)$$

where $P(\mathbf{x}|\theta)$ is obtained from the absolute square of the N-particle wave function, $|\psi_\theta(\mathbf{x})|^2$, and

$$\zeta_{\mathfrak{n}} \coloneqq \frac{N!}{\prod_{j=0}^{N_p+1} \mathfrak{n}_j!}, \quad \int_A d\mathbf{x} \coloneqq \int_{A_{j_1}} dx_1 \int_{A_{j_2}} dx_2 \cdots \int_{A_{j_N}} dx_N.$$

Also, $H(N, N_p)$ is a set of the different ways of selecting N elements out of $\{A_j : j = 0, 1, \ldots, N_p + 1\}$ allowing for duplication, i.e., a set of all absorption images that can be realized. The integration part gives the probability of finding the first particle in the range A_{j_1}, the second particle in the range A_{j_2}, and so on. Note that the set $A = \{A_{j_1}, \ldots, A_{j_N}\}$ is in an ascending order, $j_1 \leqslant j_2 \leqslant \cdots \leqslant j_N$, and that is why $\zeta_{\mathfrak{n}}$ is multiplied to consider the indistinguishability of particles. In short, the A is an area in the N-dimensional space of $(x_1, \ldots, x_N)$, where any element leads to the same absorption image, $\mathfrak{n}$. Finally, using Eq. (16), the CFI for the absorption imaging is obtained as

$$F(\theta) \quad = \sum_{\mathfrak{n}\in H(N,N_p)} \frac{1}{P(\mathfrak{n}|\theta)} \left(\frac{dP(\mathfrak{n}|\theta)}{d\theta}\right)^2, \qquad (17)$$

which determines the precision level for estimating θ of ρ_θ from the results of absorption imaging method.

For example, let us suppose $N = 5$ and $N_p = 3$, that is, 5 particles and three pixels, thus a case of very low resolution. Then the integration area, A, corresponding to an absorption image $\mathfrak{n} = (1, 1, 2, 1, 0)$ will be $\{A_0, A_1, A_2, A_2, A_3\}$ and $\zeta_{\mathfrak{n}} = 5!/(1!1!2!1!) = 60$. In a similar manner, any absorption image has a corresponding representation of A. The probability of attaining $(1, 1, 2, 1, 0)$ as an absorption image can be calculated as

$$60 \times \int_{-\infty}^{a_0} dx_1 \int_{a_0}^{a_1} dx_2 \int_{a_1}^{a_2} dx_3 \int_{a_1}^{a_2} dx_4 \int_{a_2}^{a_3} dx_5\,P(\mathbf{x}|\theta),$$

where $P(\mathbf{x}|\theta) = |\psi_\theta(\mathbf{x})|^2$ and the integral for each range is implemented with the repetition indicated by $(1, 1, 2, 1, 0)$. Also, $H(N, N_p)$ is a set of all absorption images that can be realized by 5 particles with $3 + 2$ ranges

$$\{(5, 0, 0, 0, 0), (4, 1, 0, 0, 0), \cdots (0, 0, 0, 0, 5)\}$$

with the total number of elements $\frac{(N+N_p+1)!}{(N_p+1)!N!} = 126$. Now we have everything in hand to calculate the CFI for the absorption imaging. Later on, we will check by numerical simulation that the CFI of the single-shot measurement with finite resolution, Eq. (17), converges to the CFI provided by the wave function, Eq. (13), upon decreasing Δx_p.

C. Fisher information of the Bethe ansatz

We suppose that the interaction strength c is a target parameter to be estimated and the system size L is a known resource parameter that we can directly control in the LL model. The L is a resource in a sense that it serves a possibility of enhancing measurement precision of another parameter c. Note that we focus on the estimation of a Hamiltonian parameter

that is encoded into a state while it is being realized as an eigenstate of the Hamiltonian rather than by evolving through a unitary evolution, e.g., Mach-Zehnder or Ramsey interferometry. Hence we use Eq. (11) and Eq. (13) in Sec. III A to calculate the QFI and the CFI directly from the wave functions. Since the wave functions in Eq. (3) and Eq. (6) are unnormalized, the expressions of QFI and CFI, Eq. (11) and Eq. (13), need to be rewritten in terms of unnormalized wave functions:

$$\mathfrak{F} = \frac{4}{\mathcal{N}^2}\left[\int d\mathbf{x}\left|\frac{d\tilde{\psi}}{dc}\right|^2 - \frac{1}{\mathcal{N}^2}\left|\int d\mathbf{x}\,\tilde{\psi}^*\frac{d\tilde{\psi}}{dc}\right|^2\right], \quad (18a)$$

$$F = \frac{4}{\mathcal{N}^2}\left[\int d\mathbf{x}\left(\frac{d|\tilde{\psi}|}{dc}\right)^2 - \left(\frac{d\mathcal{N}}{dc}\right)^2\right]. \quad (18b)$$

If $\tilde{\psi}$ is a normalized wave function, $\mathcal{N} = 1$, then Eq. (11) and Eq. (13) are recovered.

The expansion of the QFI in Eq. (18a) with respect to the Bethe ansatz solution under periodic boundary condition, Eq. (3), is the following:

$$\mathfrak{F}_p = \frac{4}{\mathcal{N}^2}\left[\sum_{P,Q}\left(\frac{dA^*(P)}{dc}\frac{dA(Q)}{dc}\mathfrak{I}(k_P - k_Q) + i\frac{dA^*(P)}{dc}A(Q)\sum_{l=1}^{N}\frac{dk_{Q_l}}{dc}\mathfrak{I}_l^1(k_P - k_Q)\right.\right.$$

$$\left.\left. - iA^*(P)\frac{dA(Q)}{dc}\sum_{l=1}^{N}\frac{dk_{P_l}}{dc}\mathfrak{I}_l^1(k_P - k_Q) + A^*(P)A(Q)\sum_{m,n=1}^{N}\frac{dk_{P_m}}{dc}\frac{dk_{Q_n}}{dc}\mathfrak{I}_{mn}^{11}(k_P - k_Q)\right)\right.$$

$$\left. - \frac{1}{\mathcal{N}^2}\left|\sum_{P,Q}\left(A^*(P)\frac{dA(Q)}{dc}\mathfrak{I}(k_P - k_Q) + iA^*(P)A(Q)\sum_{l=1}^{N}\frac{dk_{Q_l}}{dc}\mathfrak{I}_l^1(k_P - k_Q)\right)\right|^2\right], \quad (19)$$

where we introduced the notation

$$\mathfrak{I}_{mn}^{\alpha\beta}(\lambda) := \int_0^L dx_N \int_0^{x_N} dx_{N-1}\cdots \int_0^{x_2} dx_1\, x_m^\alpha x_n^\beta e^{-i\sum_{j=1}^{N}\lambda_j x_j}, \quad (20)$$

as an abbreviation to avoid the repetition of similar integrals, and where the indices of $\mathfrak{I}$ are integers satisfying $1 \leqslant m, n \leqslant N$ and $\alpha, \beta \geqslant 0$. Also, x_m^α (x_n^β) means x_m (x_n), i.e., the position of mth (nth) particle, to the power of α (β) and if the each power, α or β, is zero, then the corresponding subscript, m or n, needs not be specified, thus it can be omitted. The λ in Eq. (20) indicates $\{\lambda_1, \ldots, \lambda_N\}$ and likewise, k_P and k_Q are the short notations for the permuted set of quasimomenta, $\{k_{P_1}, \ldots, k_{P_N}\}$ and $\{k_{Q_1}, \ldots, k_{Q_N}\}$, respectively. Hence all of $\mathfrak{I}(k_P - k_Q)$, $\mathfrak{I}_l^1(k_P - k_Q)$, and $\mathfrak{I}_{mn}^{11}(k_P - k_Q)$ in Eq. (19) are clearly defined.

The replacement of $\sum_{P,Q} \to \sum_{\epsilon,\delta}\pi_\epsilon\pi_\delta\sum_{P,Q}$, $A(P) \to A(\epsilon, P)$, $A(Q) \to A(\delta, Q)$, $k_{P_j} \to \epsilon_j k_{P_j}$, and $k_{Q_j} \to \delta_j k_{Q_j}$, and modifying the definition of $\mathcal{N}$ from Eq. (5) to Eq. (8) lead to the corresponding QFI for the hard-wall boundary condition, $\mathfrak{F}_h$. Refer to Eqs. (3) and (6) for the definitions of the replaced symbols above. The CFI in Eq. (18b) can be similarly expanded under each boundary condition.

In Eq. (19), it is obvious from the definitions that $\mathcal{N}$, $A(P)$, $A(Q)$, and the multiple integral parts in Eq. (20) all

depend on the difference between any two quasimomenta in $\{k_1, k_2, \ldots, k_N\}$, not on the values of quasimomenta themselves. Furthermore, from the Bethe equations in Eq. (4) under the periodic boundary condition, we can derive the following analytical expression for the derivative of quasimomenta with respect to c:

$$\frac{dk_j}{dc} = \sum_{a=1}^{N}[\mathbf{H}^{-1}]_{ja}\sum_{l=1}^{N}\frac{2(k_a - k_l)}{c^2 + (k_a - k_l)^2}, \quad (21)$$

where the matrix $\mathbf{H}$ is from Eq. (5) and relies on the difference between any two quasimomenta. This shows that dk_{P_j}/dc or dk_{Q_j}/dc in Eq. (19) also depends on a set of $N - 1$ elements $\{k_1 - k_2, k_2 - k_3, \ldots, k_{N-1} - k_N\}$, not on $\{k_1, k_2, \ldots, k_N\}$. The $dA(P)/dc$ and $dA(Q)/dc$ are functions of $\{k_1 - k_2, k_2 - k_3, \ldots, k_{N-1} - k_N\}$, thus the QFI in Eq. (19) is a function of $k_j - k_{j+1}$ $\forall j$. This implies that $\mathfrak{F}_p$, and also F_p, are invariant under the translation of the whole quantum numbers $\{I_1, \cdots, I_N\} \to \{I_1 + J, \cdots, I_N + J\}$, since $\{k_j - k_{j+1}|j = 1, 2, \cdots, N - 1\}$ is completely

determined by $\{I_j - I_{j+1} | j = 1, 2, \cdots, N - 1\}$. The sum over permutations, $\sum_P \sum_Q$, makes $\mathfrak{F}_p$ and F_p invariant if one reverses the order of entries in $\{k_1 - k_2, k_2 - k_3, \cdots, k_{N-1} - k_N\}$, too. An example for this case is a transition from a state with quantum numbers $[I_1 = -1, I_2 = 0, I_3 = 2]$ to a state with $[I_1 = -1, I_2 = 1, I_3 = 2]$. Note here that $\{I_1 - I_2 = -1, I_2 - I_3 = -2\}$ is reversed to $\{I_1 - I_2 = -2, I_2 - I_3 = -1\}$, and so, similarly, is $\{k_1 - k_2, k_2 - k_3\}$.

On the other hand, under the hard-wall boundary condition, the derivative of the Bethe equations in Eq. (7) gives

$$\frac{dk_j}{dc} = \sum_{a=1}^{N} [\mathbf{H}^{-1}]_{ja}$$
$$\times \sum_{l \neq a} \left[\frac{k_a - k_l}{c^2 + (k_a - k_l)^2} + \frac{k_a + k_l}{c^2 + (k_a + k_l)^2} \right], \quad (22)$$

where the matrix $\mathbf{H}$ is from Eq. (A12). This means that the QFI, and also the CFI, for the hard-wall geometry, depend on both of $\{k_j - k_{j+1} | j = 1, 2, \cdots, N - 1\}$ and $\{k_j + k_{j+1} | j = 1, 2, \cdots, N - 1\}$, in short, $\{k_j | j = 1, 2, \cdots, N\}$. Thus there is no invariance of $\mathfrak{F}_h$ and F_h with respect to the operations on quantum numbers described above.

There are several difficulties in the calculation of QFI and CFI with respect to the LL eigenstates. One of them is that we encounter computing the multiple integrals in the domain D' as in Eq. (20). These multiple integrals appear in the calculation of the norm, scalar product [57–59], and correlation function [60] with respect to the Bethe ansatz. Using the simple calculative techniques specified in Ref. [60]

$$\int dx \, x^p \, e^{ikx} = -p! \left(\frac{i}{k} \right)^{p+1} e^{ikx} \sum_{s=0}^{p} \frac{(-ikx)^s}{s!},$$

we can reduce the computational time when compared to purely letting the integrals be implemented by Monte Carlo simulation. Another severe issue arises in the sums which are inherent in the Bethe ansatz: $(\sum_P)^2$ or $(\sum_\epsilon \sum_P)^2$ for the periodic or hard-wall boundary conditions, respectively. This results in a huge algorithmic complexity proportional to $\sim N!^2$ or $\sim 2^{2N} N!^2$ for each boundary condition. To avoid this complexity, we restrict ourselves to a small number of particles in the numerical calculation of Fisher information.

IV. ANALYSIS OF THE FISHER INFORMATION

Since the CFI based on a wave function is expected to be attainable by the absorption imaging method, which is later shown, we calculate the QFI and the CFI for the interaction strength c imprinted on the eigenfunctions of the LL Hamiltonian to see how precisely the parameter can be determined by implementing the single-shot measurement on the LL stationary states. We investigate how under different boundary conditions the Fisher information for c behaves according to the system variables, e.g., c, L, and N, and the types of low-lying elementary excitations. The Fisher information is numerically computed by Eq. (19) and its adjusted version for the hard-wall boundary condition.
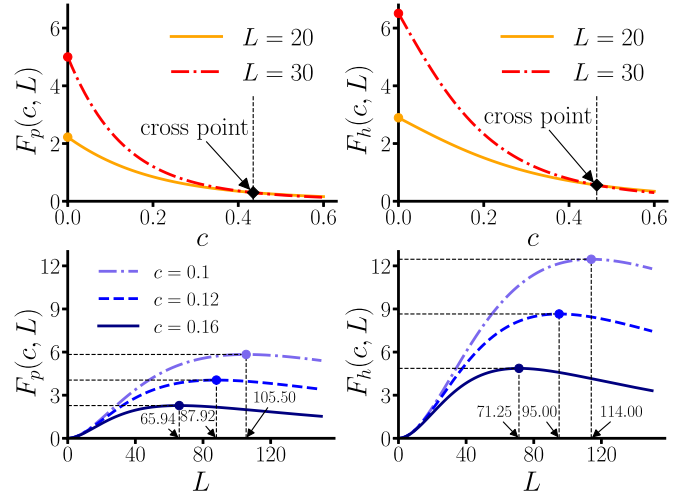

FIG. 2. The CFI for c of the $N = 2$ LL ground state as a function of the system variables c and L. In each row, the left plot is for the periodic boundary condition, and the right plot is for the hard-wall boundary condition. For $N = 2$, both ground-state wave functions are real-valued, thus the CFI, $F(c, L)$, is equal to the QFI, $\mathfrak{F}(c, L)$. In the upper row, the maximum value at $c = 0$ is $L^2/180 \simeq 0.0056 L^2$ for $F_p(c, L)$ and $L^2(-855 + 60\pi^2 + 4\pi^4)/(180\pi^4) \simeq 0.0072 L^2$ for $F_h(c, L)$. In the lower row, the maximum points appear at $c L_{\max} \simeq 10.55$ for $F_p(c, L)$ and $c L_{\max} \simeq 11.40$ for $F_h(c, L)$. Hence, for larger c, the optimal system size $L_{\max}$ appears at a smaller value. Also, note that the hard-wall geometry helps to enhance the Fisher information in excess of its ring-geometry counterpart.

A. Ground states

First we examine the case of the LL ground states that have the least number of interacting particles, $N = 2$. Under the periodic boundary condition, the quantum numbers for the ground state, $[I_1 = -1/2, I_2 = 1/2]$, lead to symmetrically distributed quasimomenta, $k_2 = -k_1$, which make the wave function in Eq. (3) real-valued. Under the hard-wall boundary condition, the set of quantum numbers for the ground state is $[I_1 = 1, I_2 = 2]$ and results in the corresponding quasimomenta satisfying $0 < k_1 < k_2$. Due to the form of Bethe ansatz that has the wave components reflected from the hard-wall, the wave function in Eq. (6) is real-valued, too. In conclusion, the QFI and the CFI are completely equal for the $N = 2$ LL ground states.

Figure 2 shows how the CFI behaves according to c (upper row) or L (lower row) in the case above. In each row, the left plot shows the CFI for the periodic boundary condition, $F_p(c, L)$, and the right plot shows the CFI for the hard-wall boundary condition, $F_h(c, L)$, and they can be compared in parallel, with the same scales of axes.

In the upper row, we can see a rapid and monotonic decrement of CFI as the interaction coupling c increases, exhibiting a maximum at $c = 0$. Larger L leads to higher CFI under the same value of c, but this is reversed after some value of c. Also, note that $F_p(c, L) \leqslant F_h(c, L)$. In the upper left plot, the maximum value can be computed as $F_p(c = 0, L) = L^2/180 \simeq 0.0056 L^2$ by inserting the small-c approximation $k_j = q_j \sqrt{2c/L} + O(c)$, where the q_j are the zeros of Hermite polynomial of order N, $H_N(q)$ [10],

into the $F_p(c, L)$ and taking the limit $c \to 0$. In the upper right plot, $k_1 = \pi/L - \sqrt{c/(2L)} + O(c)$ and $k_2 = \pi/L + \sqrt{c/(2L)} + O(c)$ are inserted into $F_h(c, L)$, and then taking the limit $c \to 0$ gives $F_h(c = 0, L) = L^2(-855 + 60\pi^2 + 4\pi^4)/(180\pi^4) \simeq 0.0072L^2$. When c is extremely large, the quasimomenta k_j are getting less relevant to the c since $k_j \to 2\pi I_j/L$ or $k_j \to \pi I_j/L$ up to the first dominant term under the periodic or hard-wall boundary condition, thus the distinguishability of the ground state with respect to c decreases.

The lower row in Fig. 2 shows the variation of CFI as the system size L increases. Both of $F_p(c, L)$ and $F_h(c, L)$ rise from 0 at $L = 0$, reach their maxima at $L = L_{\max}$, and finally decrease gradually. As mentioned, the CFI is a quadratic function of L when $c = 0$ and monotonically increases as $L \to \infty$. For any nonzero value of $c > 0$, however, the region of the quadratic increase with L of the CFI moves to a regime of smaller L, and the CFI begins to decrease after reaching a maximum at $L = L_{\max}$, thus it is confirmed that the interaction overall deteriorates the measurement precision. The maximum of CFI gets lower as c increases and its position $L_{\max}$ moves to the left accordingly. We have numerically obtained this optimal value of L by solving $dF_{p,h}(c, L)/dL|_{L=L_{\max}} = 0$: $cL_{\max} \simeq 10.55$ for $F_p(c, L)$ and $cL_{\max} \simeq 11.40$ for $F_h(c, L)$. In short, the optimal system size $L_{\max}$ appears at a smaller value for a larger c. Here we also note that $F_p(c, L) \leqslant F_h(c, L)$, where the maximal value of $F_h(c, L)$ is roughly two times larger than the one of $F_p(c, L)$ for the same c.

In most cases, the Fisher information is dependent on a target parameter, which leads to inhomogeneous estimation precision over the range of the target parameter. In other words, the precision that would be obtained if the true θ were θ_1 can be larger or smaller than the one that would be attained if θ were a different value θ_2. An exception to this is the estimation of the mean of a Gaussian distribution, where the Fisher information for the mean does not depend on the mean itself and is given by the inverse of the variance. Similarly, in Mach-Zehnder interferometry (MZI), one often tries to estimate the θ encoded by unitary operator, e.g., $e^{-i\theta\hat{\sigma}_y}$, to a general quantum state $\rho_0 = (I + \vec{s}_0 \cdot \vec{\sigma})/2$, where $\vec{s}_0 \in \mathbf{R}^3$ with $|\vec{s}_0| \leqslant 1$ and $\vec{\sigma}$ is the vector of Pauli matrices, $\{\sigma_x, \sigma_y, \sigma_z\}$. The QFI in this case depends only on $\vec{s}_0$, but not on θ, while the CFI for the measurement of population imbalance between two arms of interferometer, which is the typical choice in MZI, is dependent on θ as well as the initial state parameter $\vec{s}_0$. For pure states, there exists a class of optimal $\vec{s}_0$ which lets the CFI saturate the QFI. See Refs. [38,40] for further details. On the other hand, unlike the typical (linear) MZI above, where the parameter to be estimated appears as a multiplicative factor to the generator of unitary evolution, the dependence of a Hamiltonian on the parameter can be more general [61]. In this case, the QFI can rely on the target parameter itself. In the present example of LL model, the system size L plays the role of initial state parameter other than the target parameter c, and the equality of QFI and CFI is guaranteed for the $N = 2$ ground state. Here the QFI for c has the dependence on c as in the metrology with the general Hamiltonian above, thus the optimal L, $L_{\max}$, relies on the value of c, which is quite different from the linear MZI case. Also, our metrological protocol does not use any unitary operator to encode the target
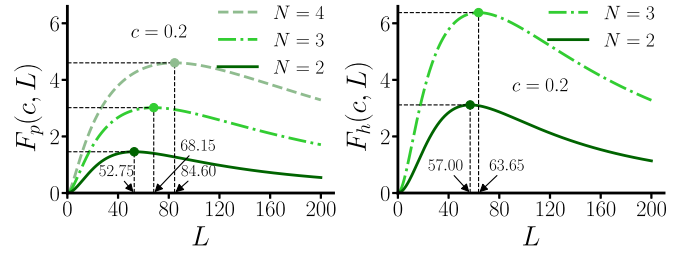

FIG. 3. The CFI for c of the LL ground state as a function of L, where $c = 0.2$ and the particle number is slightly increased from $N = 2$. The left plot is for the periodic boundary condition, in which the ground-state wave function is real-valued for all N. The right plot is for the hard-wall boundary condition, in which the ground-state wave function is real-valued for even N or is purely imaginary-valued for odd N. In any case, the CFI is equal to the QFI. As N grows, the CFI shows a significant enhancement over the whole range of L maintaining its behavioral pattern and the $L_{\max}$, at which the CFI is maximal, moves right: $cL_{\max} \simeq 10.55, 13.63, 16.92$ for $F_p(c, L)$ and $cL_{\max} \simeq 11.40, 12.73$ for $F_h(c, L)$. For the same N, the system with hard-wall geometry exhibits a much higher CFI.

parameter and that is why the QFI does not have a cyclical property with respect to c [40].

In Fig. 3 the particle number is raised up to $N = 4$ in the case of $F_p(c, L)$ (left plot), while up to $N = 3$ in the case of $F_h(c, L)$ (right plot), where $c = 0.2$ is supposed in all plots. The wave function in Eq. (3) is real-valued for any N if the quasimomenta, $\{k_1, k_2, \ldots, k_N\}$, are symmetrically distributed around 0 and the ground state satisfies this condition. On the other hand, the wave function in Eq. (6) is real-valued for even N and purely imaginary-valued for odd N. Thus, as far as ground states are concerned, the CFI and the QFI are equal for any N. As N increases, the CFI increases over the whole range of L and the $L_{\max}$ increases accordingly: $cL_{\max} \simeq 10.55, 13.63, 16.92$ for $F_p(c, L)$ and $cL_{\max} \simeq 11.40, 12.73$ for $F_h(c, L)$. Also, the advantage of the hard-wall geometry for the CFI is clear from Fig. 3, when keeping N fixed.

B. Excited states

For low-lying excitations, there are two branches of elementary excitations in the LL model [7]: The type I and the type II varieties, which are distinguished by the energy-momentum dispersion relation. For a given total momentum, type I excited state is the state of maximal energy and type II excited state is the state of minimal energy. Those are also identified by two different types of the transition of quantum numbers from $I_{j=1,\ldots,N} = -(N-1)/2 + j - 1$ or $I_{j=1,\ldots,N} = j$, which represents the distribution of quantum numbers of the ground state under periodic or hard-wall boundary condition. For the periodic boundary condition, $I_{j=1,\ldots,N-1} = -(N-1)/2 + j - 1$ and $I_N = (N-1)/2 + q$ with an integer $q \geqslant 1$ represent the type I excited states. The type II excited states are represented by $I_{j<q} = -(N-1)/2 + j - 1$ and $I_{j\geqslant q} = -(N-1)/2 + j$ with an integer $1 \leqslant q \leqslant N-1$. The type II excitation with $q = 1$ is in fact classified as the third type excitation called Umklapp excitation, but for our discussion this can be understood as an extension of the type
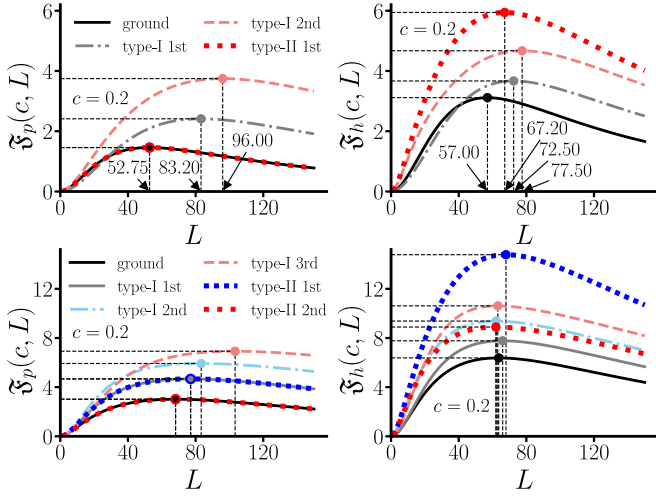
FIG. 4. The QFI for c of the LL ground or excited state as a function of L, where $c = 0.2$. The upper row is for $N = 2$, and the lower row is for $N = 3$. In each row, the left plot is for the periodic boundary condition, and the right plot is for the hard-wall boundary condition. Upper left: The type I excited states give higher QFI as the energy increases, but the type II excited state, $[I_1 = 0.5, I_2 = 1.5]$ (red dotted), gets back to the level of ground state, $[I_1 = -0.5, I_2 = 0.5]$ (black solid). Upper right: The system with hard-wall geometry similarly exhibits higher QFI as it gets more type I excited, but now the type II excited state, $[I_1 = 2, I_2 = 3]$ (red dotted), shows much higher QFI than its type I counterpart (light-red dashed). Lower left: The QFI of any type II excited state is always smaller than that of its type I counterpart and reproduces the QFI of ground or type I excited state. The values of L_{max} are 68.15 (black solid), 77.05 (gray solid), 83.3 (light-blue dash-dot), 103.35 (light-red dashed), 77.05 (blue densely dotted), and 68.15 (red dotted). Lower right: The type II excited state with $[I_1 = 1, I_2 = 3, I_3 = 4]$ (blue densely dotted) gives the best QFI, but another one with $[I_1 = 2, I_2 = 3, I_3 = 4]$ (red dotted) gives lower QFI than its type I counterpart (light-red dashed). The values of L_{max} are 63.65 (black solid), 66.00 (gray solid), 62.15 (light-blue dash-dot), 63.10 (light-red dashed), 67.95 (blue densely dotted), and 62.00 (red dotted).

II excitation. For the hard-wall boundary condition, the total momentum is not defined since it is not a conserved quantity. However, we can find an appropriate alternative resembling the total momentum [21]: $P = (\pi/L) \sum_{j=1}^{N} (I_j - j + 1)$, with which the energy-momentum dispersion relation can be established. Then the type I excitation is defined by $I_{j=1,...,N-1} = j$ and $I_N = N + q$ with an integer $q \geqslant 1$. The type II excitation is expressed as $I_{j<q} = j$ and $I_{j \geqslant q} = j + 1$ with an integer $1 \leqslant q \leqslant N - 1$.

Figure 4 shows the QFI for c of the LL ground or excited state as a function of L, where $c = 0.2$. The upper row is for $N = 2$ and the lower row is for $N = 3$. In each row, the left plot is for the periodic boundary condition and the right plot is for the hard-wall boundary condition. A pair of type I and type II excited states that have the same total momentum is similarly colored, i.e., light-red dashed $\leftrightarrow$ red dotted and light-blue dash-dot $\leftrightarrow$ blue densely dotted. Each state is denoted by a set of quantum numbers. As explained, $\mathfrak{F}_p(c, L)$ is equal to $F_p(c, L)$ when the quantum

numbers are symmetric around 0, because the wave function is real-valued then. When $N = 2$, however, $\mathfrak{F}_p(c, L) = F_p(c, L)$ holds for any set of quantum numbers due to the invariance of $\mathfrak{F}_p(c, L)$ and $F_p(c, L)$ with respect to the translation of quantum numbers. For example, $[I_1 = 0.5, I_2 = 2.5]$ can be translated into $[I_1 = -1, I_2 = 1]$ while keeping $\mathfrak{F}_p(c, L)$ and $F_p(c, L)$ constant, and the wave function for $[I_1 = -1, I_2 = 1]$, which is artificially made symmetric around 0, is clearly real-valued. Thus it is concluded that $\mathfrak{F}_p(c, L) = F_p(c, L)$ even for $[I_1 = 0.5, I_2 = 2.5]$. When $N > 2$, there are many states whose quantum numbers cannot be made symmetric around 0, hence $\mathfrak{F}_p(c, L) > F_p(c, L)$ by Eq. (14). However, in current regimes of parameters, the difference is confirmed to be minor, and we ignore it in the following discussion. On the other hand, $\mathfrak{F}_h(c, L) = F_h(c, L)$ is guaranteed for all N since the wave function in Eq. (6) is always either of real-valued or pure imaginary-valued, as discussed in Sec. III A. We can see in Fig. 4 how the QFI for c behaves as the state shifts from the ground state to the different excited states.

In the upper left plot, as the energy increases along the type I excitations, the $\mathfrak{F}_p(c, L)$ shows a higher maximum with a larger L_{max}. When the state is excited to $[I_1 = -0.5, I_2 = 1.5]$ (gray dash-dot), the $\mathfrak{F}_p(c, L)$ slightly decreases in the lower range of L, but in the upper range it shows a better improvement. The light-red dashed line is a type I excited state with $[I_1 = -0.5, I_2 = 2.5]$ and the red dotted line is its type II counterpart, $[I_1 = 0.5, I_2 = 1.5]$, with the same total momentum: $P = (2\pi/L) \sum_{j=1}^{N} I_j = 4\pi/L$. Here we see that the type II excitation worsens the QFI compared to its type I counterpart. Because of the dependence of $\mathfrak{F}_p(c, L)$ on $k_1 - k_2$, or, in other words, $I_1 - I_2$, the $\mathfrak{F}_p(c, L)$ for $[I_1 = 0.5, I_2 = 1.5]$ (red dotted) coincides with the one for $[I_1 = -0.5, I_2 = 0.5]$ (black solid). On the other hand, in the upper right plot, the $\mathfrak{F}_h(c, L)$ for a type II excited state with $[I_1 = 2, I_2 = 3]$ (red dotted), exhibits a significant improvement with higher maximum but less L_{max} compared to its type I counterpart, $[I_1 = 1, I_2 = 4]$ (light-red dashed). Contrary to the periodic boundary condition, the type II excitation contributes better to enhance the precision limit than its type I counterpart does under the hard-wall boundary condition.

The lower row in Fig. 4 produces similar results for $N = 3$ just as the upper row. In the lower left plot, the maximum of $\mathfrak{F}_p(c, L)$ and the L_{max} increase as the state is getting type I excited. However, all of type II excited states have lower QFIs than those of their type I counterparts. For a given total momentum of $P = 4\pi/L$, the QFI for a type II excited state with $[I_1 = -1, I_2 = 1, I_3 = 2]$ (blue densely dotted) is less than the one for a type I excited state with $[I_1 = -1, I_2 = 0, I_3 = 3]$ (light-blue dash-dot) and is equal to the QFI for a type I excited state with $[I_1 = -1, I_2 = 0, I_3 = 2]$ (gray solid), which is due to the invariance of $\mathfrak{F}_p(c, L)$ with respect to reversing the order in the set $\{I_1 - I_2, I_2 - I_3\}$ as explained in Sec. III C. Also, for the total momentum of $P = 6\pi/L$, the QFI for a type II excited state with $[I_1 = 0, I_2 = 1, I_3 = 2]$ (red dotted) is smaller than the one for a type I excited state with $[I_1 = -1, I_2 = 0, I_3 = 4]$ (light-red dashed) and is equal to the QFI for the ground state, $[I_1 = -1, I_2 = 0, I_3 = 1]$ (black solid), which is attributed to the invariance of $\mathfrak{F}_p(c, L)$
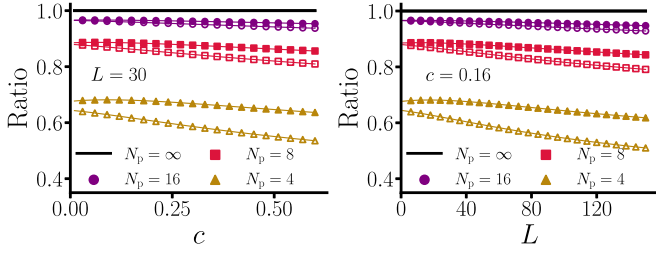
FIG. 5. The ratio between the CFI for absorption imaging with finite N_p and the $F(c, L)$, i.e., the CFI when $N_p = \infty$, in the space of system variables c and L. As the number of pixels in the absorption imaging increases, the ratio is getting closer to 1 (black solid), thus the imaging method results in the precision provided by the $F(c, L)$. For each N_p case, the line with hollow markers is for the periodic boundary condition and the line with filled markers is for the hard-wall boundary condition. When estimating a parameter from the absorption imaging method, the hard-wall geometry gives a larger CFI than that of the ring geometry and also, the former deteriorates much less as c or L grows.

with respect to the translation of quantum numbers. The lower right plot shows that the QFI for a type II excited state does not always surpass the QFI of its type I counterpart. The type II excited state with $[I_1 = 1, I_2 = 3, I_3 = 4]$ (blue densely dotted) reaches the highest QFI, but the type II excited state with $[I_1 = 2, I_2 = 3, I_3 = 4]$ (red dotted) exhibits less QFI than its type I counterpart, $[I_1 = 1, I_2 = 2, I_3 = 6]$ (light-red dashed). The $\mathfrak{F}_h(c, L)$ depends on each value of quasimomenta, not on the difference between any two quasimomenta, thus, unlike the periodic boundary condition, identical QFIs do not exist.

The differences between the two trap geometries are constituted mainly by the fact that the hard-wall geometry is more favorable to the estimation of c and that a type II excitation leads to a further enhancement of the precision limit under the hard-wall boundary condition.

C. Fisher information for absorption imaging

As explained, the absorption imaging is commonly implemented to investigate the characteristics of ultracold atomic systems. This method involves irradiating light to cold atomic gas from above, extracting the optical density captured by the CCD camera below the gas, and converting the optical density to the column density of atoms located above each pixel of the camera. In Sec. III B this process has been modeled as dividing the finite one-dimensional space into N_p pixels and counting the number of atoms in each pixel bin. We can calculate the CFI for this absorption imaging method and compare it to $F_p(c, L)$ or $F_h(c, L)$, which corresponds to the case when $N_p \to \infty$. Figure 5 shows the convergence of CFI for the absorption imaging as the number of pixels increases. The y axis represents the ratio between the CFI for the absorption imaging and $F(c, L)$. The $F(c, L)$ is calculated using $N = 2$ ground state in the LL model. The left plot is when L is fixed and the right plot is when c is fixed. The lines with filled markers indicate the hard-wall geometry and the lines with hollow markers represent the ring geometry. The CFI for the absorption imaging is higher in the hard-wall geometry

than in the ring geometry, while both go to the ideal limit, $F(c, L)$, as N_p increases. When c or L increases, the saturation of the CFI for the absorption imaging to the $F(c, L)$ tends to deteriorate, reflecting the Tonks-Girardeau behavior of gas in the $\gamma \to \infty$ limit. However, the hard-wall geometry shows less deterioration than the ring geometry in this region.

V. SUMMARY AND CONCLUSION

We have investigated the Fisher information of the interaction strength in the LL model by calculating it with respect to the eigenstates of the LL Hamiltonian. First we briefly reviewed the Bethe ansatz solutions of the LL model under two different boundary conditions: Periodic and hard-wall boundary conditions. Then we discussed the QFI and the CFI in terms of the wave function and the condition for the CFI to saturate the QFI. We numerically calculated the Fisher information of interaction strength using the LL eigenfunctions, i.e., the Bethe ansatz, and described its behavior in the space of system variables such as interaction strength and system size. We confirmed the negative effect of interaction on the measurement precision and, in particular, found an optimal value of system size for the estimation of interaction strength and the advantage of the hard-wall geometry over the ring geometry. All of these results were reproduced for varying number of particles and with the LL eigenstates of different energies. For the low-lying excitations, we explained the different aspects of type I and type II excited states appearing in the functional profile of Fisher information based on its invariance with respect to some symmetry operations on a set of quantum numbers. Finally, we showed that the CFI supported by the absorption imaging method converges to the wave function-based CFI as the pixel size in the model of absorption imaging improves. This demonstrates that the precision achievable by the ideal position measurement on N particles can be attained by elaborating the resolution of absorption imaging.

From the viewpoint of quantum metrology, our analysis is selecting a different metrological framework from the typical protocol, where a Hamiltonian parameter is imprinted by the unitary process on a quantum state, which is initially irrelevant to the parameter to be estimated. Here we rather try to determine the attainable precision of estimating a Hamiltonian parameter using the eigenstates of that Hamiltonian which already contain the information of the target parameter. Within this framework, instead of improving the N scaling of Fisher information, we have focused on its behavior in the parameter space and the precision limit that can be obtained by a realistic measurement, e.g., absorption imaging, which is the representative measurement to explore the ultracold atomic systems. It is expected that these results can be utilized in the technique of adaptive measurement, to enhance the estimation precision of the interaction strength in ultracold bosonic gases.

There have been numerous investigations of the LL model under two extreme limits of the the Lieb parameter γ: Weakly and strongly interacting regimes, which are defined by $\gamma \to 0$ and $\gamma \to \infty$, respectively. However, we confirmed that the optimal value of the resource parameter, i.e., system size, that maximizes the Fisher information of the target parameter, i.e., interaction strength, appears in the intermediate regime: $\gamma \sim$

$O(1)$. Hence the present results for the Fisher information, highlighting the distinguishability of the Bethe ansatz solutions for varying γ, reveal that the intermediate regime of the LL model is in fact the most intriguing one, as demonstrated by its metrological usefulness.

APPENDIX: BOSONIC GAS IN A BOX TRAP

The exact solution for N bosons in a box of length L is summarized here. The system is formulated by $\hat{H}\,\psi = E\,\psi$ with the following Hamiltonian and boundary conditions:

$$\hat{H} = -\sum_{j=1}^{N}\frac{\partial^2}{\partial x_j^2} + 2\,c\sum_{j<l}\delta(x_j - x_l), \tag{A1a}$$

$$\psi(x_1 = 0, x_2, \ldots, x_N) = \psi(x_1, \ldots, x_{N-1}, x_N = L) = 0, \tag{A1b}$$

where $c > 0$ and $\hbar = 2m = 1$ for the units. The ψ is symmetric under the exchange of arbitrary two spatial coordinates, thus, it is fully defined in the restricted real space $[0, L]^N$ once defined in the domain $D : 0 \leqslant x_1 \leqslant x_2 \leqslant \cdots \leqslant x_N \leqslant L$.

The (unnormalized) solution for the domain D is given by the Bethe ansatz of the following form [6,8,10]:

$$\tilde{\psi}(x_1, \ldots, x_N) = \sum_{\epsilon_1, \ldots, \epsilon_N}\ \sum_{P}\epsilon_1\epsilon_2\cdots\epsilon_N A(\epsilon_1 k_{P_1}, \ldots, \epsilon_N k_{P_N})\,e^{i\sum_{j=1}^{N}\epsilon_j k_{P_j} x_j},$$

$$A(\epsilon_1 k_{P_1}, \ldots, \epsilon_N k_{P_N}) = \prod_{j<l}\left(1 - \frac{i\,c}{\epsilon_j k_{P_j} + \epsilon_l k_{P_l}}\right)\left(1 + \frac{i\,c}{\epsilon_j k_{P_j} - \epsilon_l k_{P_l}}\right), \tag{A2}$$

in which ϵ_j is summed over ± 1 and P runs over all permutations of $[1, 2, \ldots, N]$. The sign of k_j is absorbed into ϵ_j to make $k_j > 0\ \forall j$ and also $k_1 < k_2 < \cdots < k_N$ is assumed without loss of generality due to the sum over P. Now one can find the corresponding energy $E = \sum_{j=1}^{N} k_j^2$ when $x_j \neq x_{j+1}$ ($x_1 < x_2 < \cdots < x_N$) and the rule of exchanging neighboring arguments of A:

$$A(\cdots, \epsilon_j k_j, \epsilon_l k_l, \ldots) = \frac{\epsilon_j k_j - \epsilon_l k_l + i\,c}{\epsilon_j k_j - \epsilon_l k_l - i\,c}A(\ldots, \epsilon_l k_l, \epsilon_j k_j, \ldots), \tag{A3}$$

which comes from the continuity of $\tilde{\psi}$ at $x_j = x_{j+1}$: $c\,\tilde{\psi}|_{x_{j+1}=x_j} = [\partial\tilde{\psi}/\partial x_{j+1} - \partial\tilde{\psi}/\partial x_j]|_{x_{j+1}=x_j}$.

The first condition in Eq. (A1b), $\tilde{\psi}(x_1 = 0, x_2, \ldots, x_N) = 0$, results in the symmetry of A under the sign reverse of its first argument:

$$A(\epsilon_j k_j, \ldots) = A(-\epsilon_j k_j, \ldots), \tag{A4}$$

and the second condition in Eq. (A1b), $\tilde{\psi}(x_1, \ldots, x_{N-1}, x_N = L) = 0$, provides the additional conditions on the k_j's:

$$e^{i\,2k_j L} = \frac{A(\cdots, -k_j)}{A(\cdots, k_j)}, \tag{A5}$$

where "$\cdots$" abbreviates the same arguments between numerator and denominator. Apply Eq. (A3) to the numerator of the right-hand side in Eq. (A5) iteratively so that $-k_j$ can be placed in the first argument. Then its minus sign can be removed due to Eq. (A4). Again apply Eq. (A3) to that numerator repeatedly to get the sign-removed k_j back to its original position, that is, to the last argument. Finally, one obtains the Bethe equations from Eq. (A5):

$$e^{i\,2k_j L} = \prod_{l\neq j}\frac{k_j + k_l + i\,c}{k_j + k_l - i\,c}\frac{k_j - k_l + i\,c}{k_j - k_l - i\,c}. \tag{A6}$$

Applying the logarithm to the both sides of Eq. (A6) leads to a systems of N real equations

$$L k_j = \pi n_j + \sum_{l\neq j}\left[\tan^{-1}\left(\frac{c}{k_j - k_l}\right) + \tan^{-1}\left(\frac{c}{k_j + k_l}\right)\right] \tag{A7}$$

with integer n_j's satisfying $1 \leqslant n_1 \leqslant n_2 \leqslant \cdots \leqslant n_N$. A different form of the Bethe equations is obtained using $\tan^{-1}(X) = \pm\frac{\pi}{2} - \tan^{-1}(1/X)$ when $X \gtrless 0$:

$$L k_j = \pi I_j - \sum_{l\neq j}\left[\tan^{-1}\left(\frac{k_j - k_l}{c}\right) + \tan^{-1}\left(\frac{k_j + k_l}{c}\right)\right], \tag{A8}$$

where $I_j = n_j + j - 1$. Note that the n_j's allow duplicate values, but the I_j's do not. For example, the ground state corresponds to $n_1 = n_2 = \cdots n_N = 1$ or $I_1 = 1, I_2 = 2, \ldots, I_N = N$.

The wave function in Eq. (A2) is not normalized yet. Gaudin conjectured the norm of the Bethe ansatz in the Lieb-Liniger model under the periodic boundary condition [10] and Korepin proved it [50]. For the current hard-wall boundary condition Eq. (A1b), we modify the Gaudin's conjecture and suggest a normalized form of Eq. (A2) as

$$\psi(x_1, \ldots, x_N) = 2^{-\frac{N}{2}} \left| \mathbf{H}(B) \right|^{-\frac{1}{2}} \sum_{\epsilon_1, \ldots, \epsilon_N} \sum_{P} \epsilon_1 \cdots \epsilon_N (-)^P \exp\left(\frac{i}{2} \sum_{j<l} \phi_{P_j,P_l}^{\epsilon_j,\epsilon_l} - \frac{i}{2} \sum_{j<l} \varphi_{P_j,P_l}^{\epsilon_j,\epsilon_l} + i \sum_{j=1}^{N} \epsilon_j k_{P_j} x_j \right), \quad (A9)$$

where $\phi_{P_j,P_l}^{\epsilon_j,\epsilon_l} := 2\tan^{-1}(\frac{c}{\epsilon_j k_{P_j} - \epsilon_l k_{P_l}})$, $\varphi_{P_j,P_l}^{\epsilon_j,\epsilon_l} := 2\tan^{-1}(\frac{c}{\epsilon_j k_{P_j} + \epsilon_l k_{P_l}})$, and $(-)^P$ is $+/-1$ for even/odd permutation(P). Also, $|\mathbf{H}(B)|$ is the determinant of the Hessian matrix of

$$B(k_1, \ldots, k_N) := \frac{L}{2} \sum_{j=1}^{N} k_j^2 - \pi \sum_{j=1}^{N} I_j k_j + \frac{1}{2} \sum_{j=1}^{N} \sum_{l \neq j} \left[\int_0^{k_j - k_l} dk \tan^{-1}\left(\frac{k}{c}\right) + \int_0^{k_j + k_l} dk \tan^{-1}\left(\frac{k}{c}\right) \right]. \quad (A10)$$

Then the norm squared of Eq.(A2) can be explicitly written as

$$\mathcal{N}^2 = 2^N \prod_{j<l} \left[1 + \frac{c^2}{(k_j - k_l)^2} \right] \left[1 + \frac{c^2}{(k_j + k_l)^2} \right] \det[\mathbf{H}(B)], \quad (A11)$$

where the entries of the Hessian matrix $\mathbf{H}(B)$ are given by

$$\left[\mathbf{H}(B) \right]_{ij} = \delta_{ij} \left\{ L + \sum_{l \neq i} \left[\frac{c}{(k_i - k_l)^2 + c^2} + \frac{c}{(k_i + k_l)^2 + c^2} \right] \right\} + (1 - \delta_{ij}) \left[-\frac{c}{(k_i - k_j)^2 + c^2} + \frac{c}{(k_i + k_j)^2 + c^2} \right]. \quad (A12)$$

We take $\mathcal{N}$ in Eq. (A11) to be the exact norm of the wave function in Eq. (A2), without mathematical rigor being applied. We checked, to justify this, empirically that Eq. (A11) fits well with the numerical result provided by evaluating $\int_0^L dx_N \int_0^{x_N} dx_{N-1} \cdots \int_0^{x_2} dx_1 |\tilde{\psi}(x_1, \ldots, x_N)|^2$.

[1] B. Paredes, A. Widera, V. Murg, O. Mandel, S. Fölling, I. Cirac, G. V. Shlyapnikov, T. W. Hänsch, and I. Bloch, Tonks–Girardeau gas of ultracold atoms in an optical lattice, Nature (London) **429**, 277 (2004).

[2] T. Kinoshita, T. Wenger, and D. S. Weiss, A quantum Newton's cradle, Nature (London) **440**, 900 (2006).

[3] H. Bethe, Zur Theorie der Metalle, Z. Phys. **71**, 205 (1931).

[4] M. Batchelor, Bethe Ansatz, in *Encyclopedia of Mathematical Physics*, edited by J.-P. Franoise, G. L. Naber, and T. S. Tsun (Academic Press, Oxford, 2006), pp. 253–257.

[5] E. H. Lieb and W. Liniger, Exact analysis of an interacting Bose gas. I. The general solution and the ground state, Phys. Rev. **130**, 1605 (1963).

[6] M. Gaudin, Boundary energy of a Bose gas in one dimension, Phys. Rev. A **4**, 386 (1971).

[7] E. H. Lieb, Exact analysis of an interacting Bose gas. II. The excitation spectrum, Phys. Rev. **130**, 1616 (1963).

[8] M. T. Batchelor, X. W. Guan, N. Oelkers, and C. Lee, The 1D interacting Bose gas in a hard wall box, J. Phys. A: Math. Gen. **38**, 7787 (2005).

[9] N. Oelkers, M. T. Batchelor, M. Bortz, and X.-W. Guan, Bethe ansatz study of one-dimensional Bose and Fermi gases with periodic and hard wall boundary conditions, J. Phys. A: Math. Gen. **39**, 1073 (2006).

[10] M. Gaudin, *The Bethe Wavefunction*, edited by J.-S. Caux (Cambridge University Press, Cambridge, 2014).

[11] Z. Ristivojevic, Excitation Spectrum of the Lieb-Liniger Model, Phys. Rev. Lett. **113**, 015301 (2014).

[12] B. Reichert, G. E. Astrakharchik, A. Petković, and Z. Ristivojevic, Exact Results for the Boundary Energy of One-Dimensional Bosons, Phys. Rev. Lett. **123**, 250602 (2019).

[13] V. Dunjko, V. Lorent, and M. Olshanii, Bosons in Cigar-Shaped Traps: Thomas-Fermi Regime, Tonks-Girardeau Regime, and in Between, Phys. Rev. Lett. **86**, 5413 (2001).

[14] G. Lang, F. Hekking, and A. Minguzzi, Ground-state energy and excitation spectrum of the Lieb-Liniger model: Accurate analytical results and conjectures about the exact solution, SciPost Phys. **3**, 003 (2017).

[15] A. Minguzzi and P. Vignolo, Strongly interacting trapped one-dimensional quantum gases: Exact solution, AVS Quantum Sci. **4**, 027102 (2022).

[16] P. P. Kulish, S. V. Manakov, and L. D. Faddeev, Comparison of the exact quantum and quasiclassical results for a nonlinear Schrödinger equation, Theor. Math Phys. **28**, 615 (1976).

[17] M. Ishikawa and H. Takayama, Solitons in a one-dimensional Bose system with the repulsive delta-function interaction, J. Phys. Soc. Jpn. **49**, 1242 (1980).

[18] B. Mottelson, Yrast Spectra of Weakly Interacting Bose-Einstein Condensates, Phys. Rev. Lett. **83**, 2695 (1999).

[19] A. Syrwid and K. Sacha, Lieb-Liniger model: Emergence of dark solitons in the course of measurements of particle positions, Phys. Rev. A **92**, 032110 (2015).

[20] W. Golletz, W. Górecki, R. Ołdziejewski, and K. Pawłowski, Dark solitons revealed in Lieb-Liniger eigenstates, Phys. Rev. Res. **2**, 033368 (2020).

[21] A. Syrwid, Quantum dark solitons in ultracold one-dimensional Bose and Fermi gases, J. Phys. B: At., Mol. Opt. Phys. **54**, 103001 (2021).

[22] O. E. Alon and L. S. Cederbaum, Pathway from Condensation via Fragmentation to Fermionization of Cold Bosonic Systems, Phys. Rev. Lett. **95**, 140402 (2005).

[23] O. V. Marchukov and U. R. Fischer, Self-consistent determination of the many-body state of ultracold bosonic atoms in a one-dimensional harmonic trap, Ann. Phys. **405**, 274 (2019).

[24] Y. Gwak, O. V. Marchukov, and U. R. Fischer, Benchmarking the multiconfigurational Hartree method by the exact wavefunction of two harmonically trapped bosons with contact interaction, Ann. Phys. **434**, 168592 (2021).

[25] W. K. Wootters, Statistical distance and Hilbert space, Phys. Rev. D **23**, 357 (1981).

[26] C. Helstrom, Minimum mean-squared error of estimates in quantum statistics, Phys. Lett. A **25**, 101 (1967).

[27] S. L. Braunstein and C. M. Caves, Statistical distance and the geometry of quantum states, Phys. Rev. Lett. **72**, 3439 (1994).

[28] M. G. A. Paris, Quantum estimation for quantum technology, Int. J. Quantum. Inform. **07**, 125 (2009).

[29] H. M. Wiseman and G. J. Milburn, *Quantum Measurement and Control* (Cambridge University Press, Cambridge, 2009).

[30] V. Giovannetti, S. Lloyd, and L. Maccone, Advances in quantum metrology, Nat. Photonics **5**, 222 (2011).

[31] V. Giovannetti, S. Lloyd, and L. Maccone, Quantum Metrology, Phys. Rev. Lett. **96**, 010401 (2006).

[32] S. L. Braunstein, Quantum Limits on Precision Measurements of Phase, Phys. Rev. Lett. **69**, 3598 (1992).

[33] V. Giovannetti, S. Lloyd, and L. Maccone, Quantum-enhanced measurements: Beating the standard quantum limit, Science **306**, 1330 (2004).

[34] S. Boixo, S. T. Flammia, C. M. Caves, and J. M. Geremia, Generalized Limits for Single-Parameter Quantum Estimation, Phys. Rev. Lett. **98**, 090401 (2007).

[35] S. Boixo, A. Datta, S. T. Flammia, A. Shaji, E. Bagan, and C. M. Caves, Quantum-limited metrology with product states, Phys. Rev. A **77**, 012317 (2008).

[36] S. Boixo, A. Datta, M. J. Davis, S. T. Flammia, A. Shaji, and C. M. Caves, Quantum Metrology: Dynamics versus Entanglement, Phys. Rev. Lett. **101**, 040403 (2008).

[37] S. Pang and A. N. Jordan, Optimal adaptive control for quantum metrology with time-dependent Hamiltonians, Nat. Commun. **8**, 14695 (2017).

[38] O. E. Barndorff-Nielsen and R. D. Gill, Fisher information in quantum statistics, J. Phys. A: Math. Gen. **33**, 4481 (2000).

[39] K. Gietka and J. Chwedeńczuk, Atom interferometer in a double-well potential, Phys. Rev. A **90**, 063601 (2014).

[40] T. Wasak, A. Smerzi, L. Pezzé, and J. Chwedeńczuk, Optimal measurements in phase estimation: Simple examples, Quant. Info. Proc. **15**, 2231 (2016).

[41] B. J. Dalton, Two-mode theory of BEC interferometry, J. Mod. Opt. **54**, 615 (2007).

[42] J. Grond, U. Hohenester, J. Schmiedmayer, and A. Smerzi, Mach-Zehnder interferometry with interacting trapped Bose-Einstein condensates, Phys. Rev. A **84**, 023619 (2011).

[43] B. J. Dalton and S. Ghanbari, Two mode theory of Bose-Einstein condensates: Interferometry and the Josephson model, J. Mod. Opt. **59**, 287 (2012).

[44] J. Javanainen and H. Chen, Optimal measurement precision of a nonlinear interferometer, Phys. Rev. A **85**, 063605 (2012).

[45] J. Javanainen and H. Chen, Ground state of the double-well condensate for quantum metrology, Phys. Rev. A **89**, 033613 (2014).

[46] G. J. Milburn, J. Corney, E. M. Wright, and D. F. Walls, Quantum dynamics of an atomic Bose-Einstein condensate in a double-well potential, Phys. Rev. A **55**, 4318 (1997).

[47] J. M. E. Fraïsse, J.-G. Baak, and U. R. Fischer, Many-body quantum metrology with scalar bosons in a single potential well, Phys. Rev. A **99**, 043618 (2019).

[48] M. H. Anderson, J. R. Ensher, M. R. Matthews, C. E. Wieman, and E. A. Cornell, Observation of Bose-Einstein condensation in a dilute atomic vapor, Science **269**, 198 (1995).

[49] M. R. Andrews, C. G. Townsend, H.-J. Miesner, D. S. Durfee, D. M. Kurn, and W. Ketterle, Observation of interference between two Bose condensates, Science **275**, 637 (1997).

[50] V. E. Korepin, Calculation of norms of Bethe wave functions, Commun. Math. Phys. **86**, 391 (1982).

[51] L. Shun-Long, Fisher information of wavefunctions: Classical and quantum, Chin. Phys. Lett. **23**, 3127 (2006).

[52] P. Facchi, R. Kulkarni, V. Man'ko, G. Marmo, E. Sudarshan, and F. Ventriglia, Classical and quantum Fisher information in the geometrical formulation of quantum mechanics, Phys. Lett. A **374**, 4801 (2010).

[53] F. Dalfovo, S. Giorgini, L. P. Pitaevskii, and S. Stringari, Theory of Bose-Einstein condensation in trapped gases, Rev. Mod. Phys. **71**, 463 (1999).

[54] K. Sakmann and M. Kasevich, Single-shot simulations of dynamic quantum many-body systems, Nat. Phys. **12**, 451 (2016).

[55] A. U. J. Lode and C. Bruder, Fragmented Superradiance of a Bose-Einstein Condensate in an Optical Cavity, Phys. Rev. Lett. **118**, 013603 (2017).

[56] A. U. J. Lode, R. Lin, M. Büttner, L. Papariello, C. Lévêque, R. Chitra, M. C. Tsatsos, D. Jaksch, and P. Molignini, Optimized observable readout from single-shot images of ultracold atoms via machine learning, Phys. Rev. A **104**, L041301 (2021).

[57] N. A. Slavnov, Calculation of scalar products of wave functions and form factors in the framework of the algebraic Bethe ansatz, Theor. Math. Phys. **79**, 502 (1989).

[58] H.-H. Chen, Exact overlaps in the Lieb-Liniger model from coordinate Bethe ansatz, Phys. Lett. B **808**, 135631 (2020).

[59] S. Sotiriadis, Non-Equilibrium Steady State of the Lieb-Liniger model: Multiple-integral representation of the time evolved many-body wave-function, arXiv:2010.03553 (2020).

[60] J. C. Zill, T. M. Wright, K. V. Kheruntsyan, T. Gasenzer, and M. J. Davis, A coordinate Bethe ansatz approach to the calculation of equilibrium and nonequilibrium correlations of the one-dimensional Bose gas, New J. Phys. **18**, 045010 (2016).

[61] S. Pang and T. A. Brun, Quantum metrology for a general Hamiltonian parameter, Phys. Rev. A **90**, 022117 (2014).